X-ray computed tomography inspection in metal additive manufacturing: the role of witness specimens

A. du Plessis [1,*], J.M. Waller [2], S.G. le Roux [1], I. Yadroitsava [3], I. Yadroitsev [3], J. Els [3], J. Prinsloo [4]

[1] Physics Department, Merriman avenue, Stellenbosch University, Stellenbosch 7602, South Africa

[2] HX5 Teammate, NASA-JSC White Sands Test Facility, Las Cruces, NM, United States

[3] Department of Mechanical Engineering, Central University of Technology, 20 President Brand street, Bloemfontein 9301, South Africa

[4] ADC Aeroswift, CSIR main campus, Meiring Naude road, Brummeria, Pretoria 0081, South Africa

* Corresponding author: anton2@sun.ac.za

Abstract

This work highlights the capabilities for high resolution X-ray computed tomography (CT) inspection of witness specimens, built alongside a complex part, in metal additive manufacturing. Such witness specimens, which can be standardized in their dimensions (fixed diameter 15 mm with cylindrical shape built in a vertical orientation), allow X-ray CT inspections with fixed and reproducible workflows. The detection of improper process parameters of the additive manufacturing system is possible as is demonstrated in this paper. It is also demonstrated how the presence of inclusions/contamination in the powder feedstock can be detected in the witness specimen. A series of Ti6Al4V witness specimens with varying porosity distributions are presented, which were part of a previous study of builds of the same set of parts on different laser powder bed fusion systems. This demonstrates how various process parameter errors are highlighted and proven to be detectable in witness specimens using standardized CT procedures. More importantly, it also allows the potential to detect layered flaws which can occur horizontally in the build plane. Such layered flaws may originate from reduced laser power, improper powder spreading or due to complete shut-down and restart of a build. A complex bracket and witness specimen cylinder were built and a layered flaw artificially induced by shutting down the system and restarting it. The positive detection of the flaw by CT in the witness rod is demonstrated. This witness rod was recently part of a round robin test and the layered flaw was successfully identified by all 10 participants in the round robin test. The witness rod and complex part were subsequently sectioned and optical microscopy reported here. This approach is especially useful for inspection of larger parts, which cannot be inspected using X-ray CT at highest possible resolution due to part size and associated CT scanning time limits.

Keywords: X-ray tomography; microCT; non-destructive testing; witness specimen; metal additive manufacturing; laser powder bed fusion; stop-start flaw; porosity

1. Introduction

Additive manufacturing (AM) is an emerging technique used to manufacture custom and complex parts for a variety of commercial applications [1–3]. One major industrial interest is the production of metal parts, which is possible for a variety of alloys with excellent mechanical properties: one popular alloy is Ti6Al4V which is used in biomedical and aerospace applications [4,5]. Laser-powder bed fusion (L-PBF) is the most widely adopted metal AM technique, which allows the manufacturing of relatively large parts with intricate, complex designs by melting layer-by-layer in a powder bed, using a laser beam. For parts built using Ti6Al4V alloy by L-PBF, the mechanical performance can be superior to conventionally manufactured cast and wrought parts [6].

However, despite the huge potential of AM, various manufacturing imperfections can occur which lead to compromised mechanical properties. Of the many types of AM imperfections possible in L-PBF parts, the most technologically important is the presence of porosity. Different forms of porosity can originate from improper process parameters [7,8], changes in the powder morphology (for example due to changing from virgin to used powder [9]), the separation of the part from the support structures during processing, and redistribution of loose powder in the form of funnels [10] as well as other causes that cannot always be predicted.

Stop-start flaws are of particular interest in this work. These flaws can be created when the system stops and restarts, for example, due to power failure. The formation of these flaws in the build plane (horizontal in plane of powder bed) is due to the shrinkage during cooling of the solidified part below the powder level during the “off-time” of the laser, creating a thicker powder layer than previous layers and which is then not entirely melted on the next layer when the laser restarts. There is also a thermal mismatch which could contribute to the observed porosity formation. A similar effect can occur if the laser power unexpectedly drops creating one or more layers which are imperfectly melted, in this case imperfect melting occurs over a large area, creating a similar flaw type. These horizontal flaws are particularly important as they can potentially extend across the entire part. Even when the extent is not large, the layered flat shape makes this kind of flaw a strong stress concentrator at its (side) edges when subjected to loading conditions. The grain evolution during solidification depends on heat flow, so stop/start flaws and other types of porosity can influence the microstructural grain growth in the vicinity of the flaw. The interaction of the pore morphology and microstructural features results in different stress distributions during loading, thus leading to unexpected damage behaviour with different types of pore shapes [11].

One of the best-suited methods to analyse AM parts for porosity or other flaw types and to optimize AM processes for porosity minimization is X-ray micro computed tomography (microCT). A recent comprehensive review of the capabilities of present day microCT for the analysis of additively manufactured parts highlights the importance of this type of non-destructive testing for process optimization and final product inspection [12]. The use of microCT is not new in the field of materials science in general [13], and in additive manufacturing in particular [14–18]. However, its wider acceptance and adoption has been limited in the AM community, mainly due to the high costs and complexity of analysis, which varies for each part.

Although the capabilities of microCT are now starting to be appreciated more widely in the AM community, there is a need for standardization of microCT inspections. This is particularly true for measurement of AM part porosity and dimensional metrology of AM parts, as mentioned in [14], in order to improve the interpretation and ultimately the proper usage of the technique as discussed in [19].

To this end we have developed a number of simplified and standardized methods for characterisation of porosity, density, and surface roughness of small coupons of 1 cm^3 cubes [20–22], and for characterisation of powder feedstock [23]. These methods include prescribed scanning parameters and subsequent image analysis steps, in order to enhance reproducibility of these analyses across different microCT systems and users. Ultimately, the hope is that these methods will be adopted by industry and formally promulgated in voluntary consensus standards published by standards development organisations such as the American Society for Testing and Materials and the International Organization for Standardization [24,25]. These methods can be used to optimize processing conditions prior to building critical parts.

In this paper, we demonstrate a similar proposed method of analysing cylindrical witness specimens and highlight the potential for standardization – fixed cylinder sizes allow recipes for CT scanning and image analysis improving the reliability of flaw detection. We demonstrate how the process-specific porosity from different pore formation mechanisms are present in both the witness specimen and the complex part built alongside it, for a series of different sets of samples. This confirms the ability to detect these types of flaws in witness specimens with the proposed scan and image analysis steps. The idea is that the witness specimen analysis will always take place with the same resolution and other scan settings, despite having a potentially larger complex part. Additionally, a witness specimen with an artificially induced stop-start flaw is analysed here in detail, including subsequent physical cross sectioning and imaging by optical microscopy. In this example, the machine was stopped and restarted 12 hours later, to artificially induce a stop-start flaw. This type of layer defect has been previously detected by microCT scans of a complex part as reported in [26]. The concept of a witness specimen is not new, and their characterization by microCT was reported previously in [27]. Witness specimens are now specified for all Class A and B metal parts fabricated using PBF and Directed Energy Deposition (DED) [28]. These parts are used in critical and semi-critical applications, whose failure would cause significant danger to personnel, loss of control, loss of a system, loss of a major component, an operating penalty, or loss of intended function. The aim of this present work is to demonstrate the suggested fixed scan parameters and a step-by-step workflow to improve the reproducibility of microCT inspections of such witness specimens. The ultimate aim of this is to allow easier usage of the microCT technique for routine quality inspections, thus improving the quality and reliability of AM parts.

2. Methods

For the series of witness specimens (rods and cubes) and complex parts (brackets) having different process porosity types, the data were taken from previously reported round robin testing encompassing a variety of L-PBF systems and different pore distributions [29]. These sets of samples were produced on a variety of different L-PBF systems with the "optimal" process parameters of each system. All samples were nearly fully-dense at >99.87% density, but the (unexpected) porosity distributions were different and are further described in [29]. More recent work on 5 mm cubes of Ti6Al4V studied the effects of varying process parameters on one system, creating a variety of porosity distributions artificially [8].

In the present work, the fabrication of a witness rod and corresponding bracket with a stop-start flaw was accomplished with an EOS-M280 L-PBF system located at the Centre for Rapid Prototyping and Manufacturing (CRPM) at the Central University of Technology, Free State, South Africa. The powder used consisted of gas atomized Ti6Al4V extra low interstitials (ELI) from TLS Technic with mean spherical particle size of 45 µm. Standard process parameters for Ti6Al4V were used as recommended by the L-PBF system manufacturer for layer thickness of 30 µm. Argon was used as a protective atmosphere with oxygen content controlled to stay below 0.12 percent.

The parts were all scanned in a microCT system at the Stellenbosch CT facility [30] similar to the complex part scans reported in [31]. The parts include a complex part (a bracket), its witness specimen, and a 1 cm^3 cubic coupon produced during the same build. The witness specimen is a 15-mm diameter cylinder built vertically up to total height of the complex part height (in this case roughly 40-mm high). The microCT scans of the witness specimen can be done at a resolution of up to 10 µm with typical microCT systems, but this requires reasonably long scan times and does not allow for mounting the sample at an angle. The selected voxel size is 25 µm which allows a larger field of view and faster scan times, with sufficient quality and resolution to allow detection of important porosity distributions as shown in this work. In the case of this work, the X-ray tomography parameters were: 200 kV, 100 µA with 0.5 mm beam filter, 250 ms acquisition time per image and no averaging of images to allow fast scan time of 20 minutes per sample.

Since the bracket was designed to be used in a load-bearing application, topology optimisation was performed to ensure optimal load-bearing capacity relative to weight, this is reported elsewhere [32]. The bracket was scanned at 46 µm initially and then close-up sections were scanned at 23 µm, with similar X-ray settings as above.

3. Results and discussion

The results are split into two sections:the first section demonstrates how the porosity distributions in the cubes, witness rods and brackets correlate with one another. This was partly reported in [30], where the focus was on differences in cubes and the witness specimens were not analysed yet. The second section focuses on the detection of an artificially created stop-start flaw present in a single witness rod.

3.1 Process porosity distributions

Several types of process-induced porosity, each with a unique mechanism responsible for its formation, are clearly distinguishable in the microCT scans of the samples made by different commercial L-PBF systems as described in [30]. In that previous work, contour pores, lack of fusion pores and keyhole pores (subsurface at the top surface only) were detected in the 1 cm^3 cubes, for example. These were unexpected at the time, which highlights the potential for microCT to add value in detection of process errors and for process optimization or refinement.

The presence of these same pore types in the associated complex brackets made by the same L-PBF system was also confirmed by microCT scans, though with less clarity in places due to poorer resolution of the brackets. In this paper, microCT scans of witness rods confirm the presence of these same pore types and pore distributions and show that each distribution type can be positively detected in this type of sample. Figures 1,2 and 3 show the examples of contour pores, lack of fusion pores and keyhole pores (at the top surface only) respectively. Different 3D views are used to illustrate the presence of the same signature porosity in each set of samples. The importance here is that the witness specimens can be used to check when slight power drops might create lack of fusion pores in a series of layers. Figure 1 shows contour porosity which is just below the surface at all vertical walls and is clearly seen in the top view of the witness specimen in Figure 1(d).

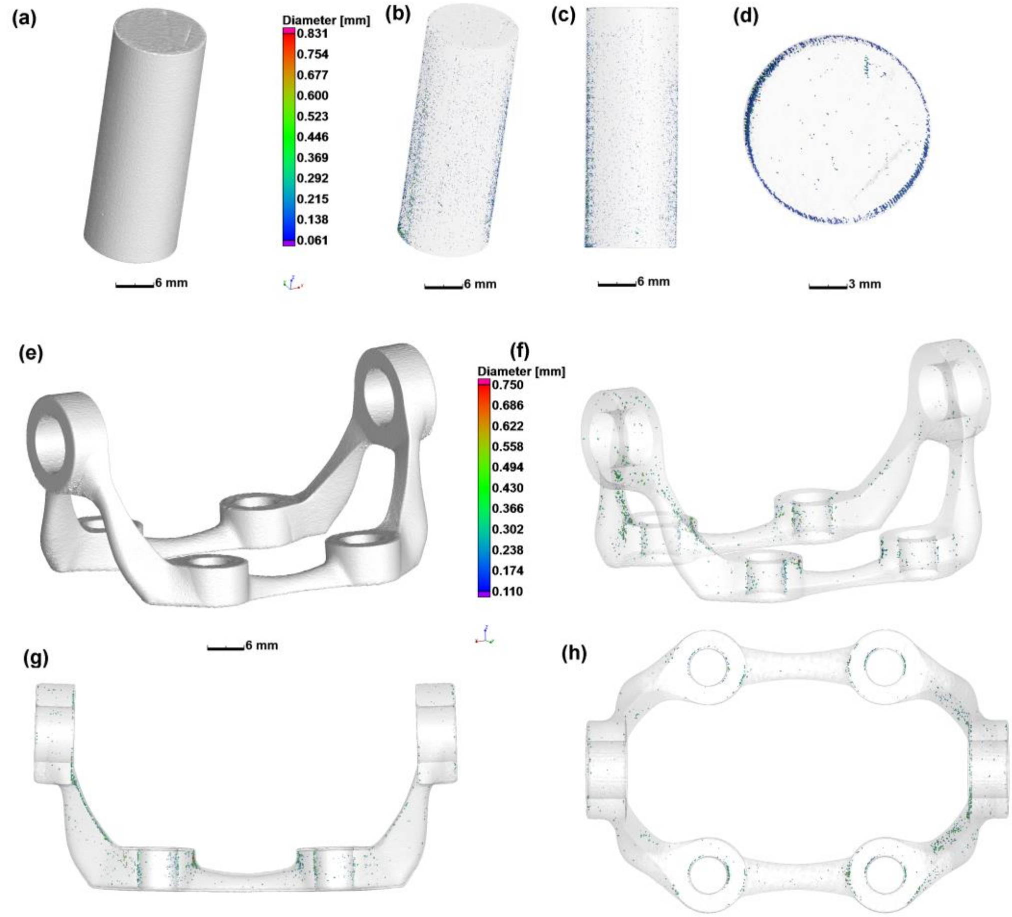

Figure 1: Process-induced porosity detected in both witness specimen and complex part, demonstrated here for contour porosity at end of scan tracks. Views shown of witness specimen (a) of surface view, (b) transparent angled view, (c) transparent side view and (d) transparent top view. View of bracket shown of (e) surface view, (f) transparent angled view, (g) transparent side view and (h) transparent top view.

Figure 2 shows lack of fusion porosity and in the witness specimen as seen in Figure 2(c) in a side view, the lack of fusion porosity is not uniformly spread across the build height. More porosity is present near the bottom of the witness specimen in this case. In the associated bracket, this difference is not clear (see Figure 2(f) for side view). This is presumably due to additional pore formation mechanisms at work in the complex part. The build strategy, the presence or absence of supports, powder delivery and part orientation on the plate have to be analysed as well as process parameters.

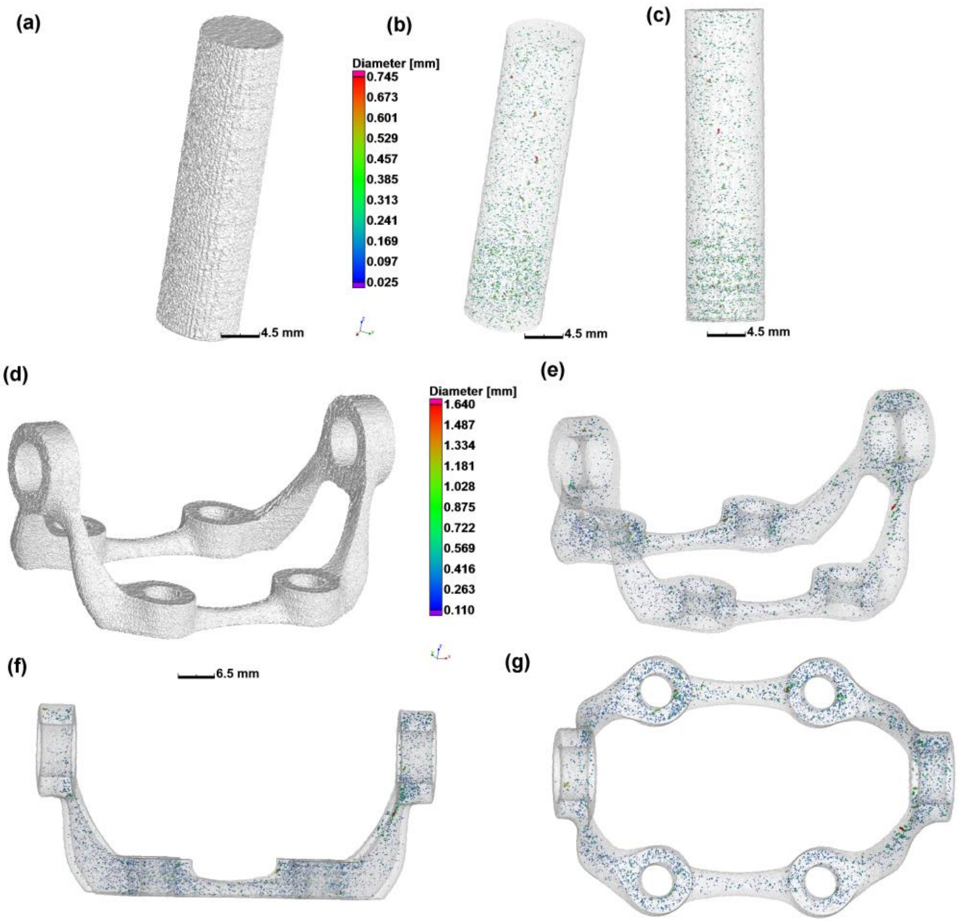

Figure 2: Process-induced porosity detected in both witness specimen and complex part, demonstrated here for lack of fusion porosity. Views shown of witness specimen (a) of surface view, (b) transparent angled view and (c) transparent side view. View of bracket shown of (d) surface view, (e) transparent angled view, (f) transparent side view and (g) transparent top view.

Figure 3 shows an example of keyhole mode pores at the top surface only, this is best seen in the witness specimen in a side view as in Figure 3(c). It is also seen in Figure 3(f) that the same type of pores are present in the bracket at horizontal top-facing surfaces.

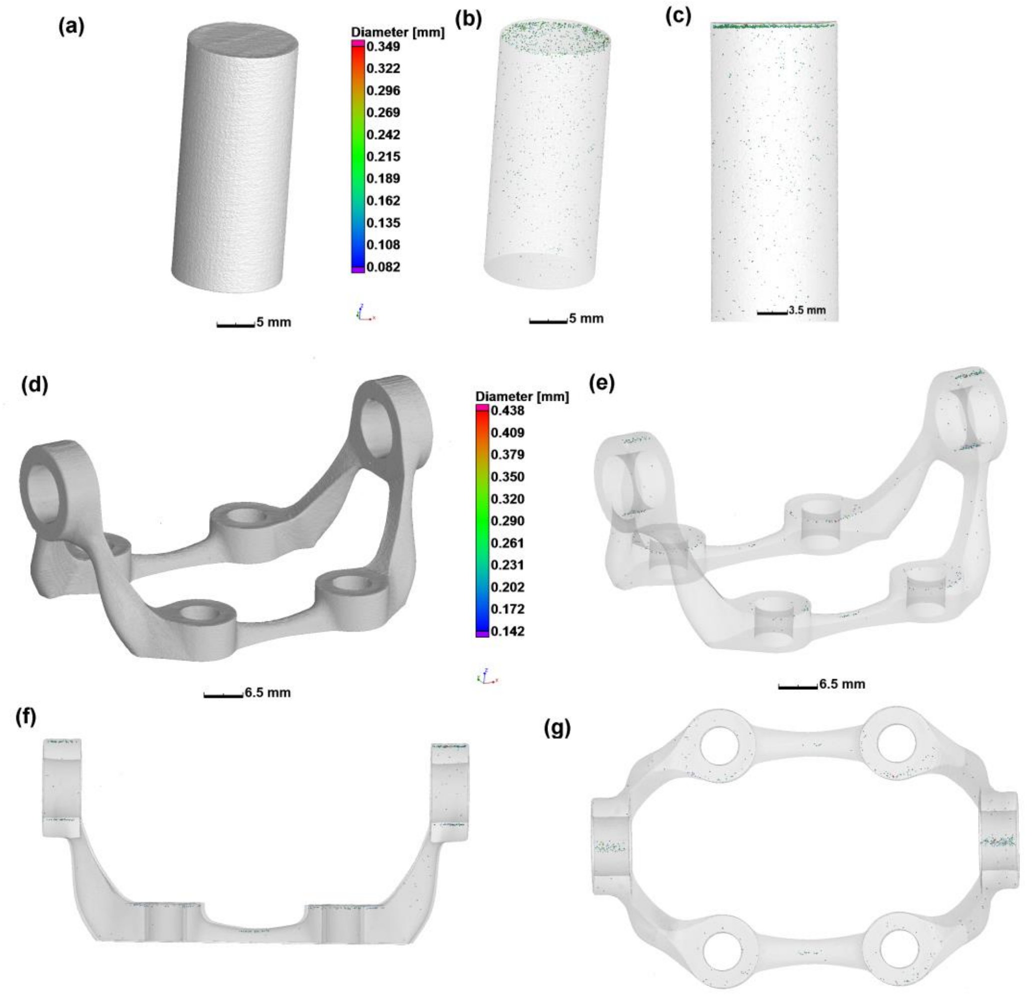

Figure 3: Process-induced porosity detected in both witness specimen and complex part, demonstrated here for keyhole mode porosity under top surface. Views shown of witness specimen (a) of surface view, (b) transparent angled view and (c) transparent side view. Views of bracket shown of (d) surface view, (e) transparent angled view, (f) transparent side view and (g) transparent top view.

In Figure 4 is shown a different set of samples with less porosity but clearly the witness specimen shows layered porosity – a particularly worrying form of porosity. When inspecting the associated bracket closely at a height corresponding to the appearance of the lower layer of porosity seen in the witness rod, this layered porosity is also detected in the in-plane CT slice data (Figure 4 (b)), and was missed in out-of-plane CT slice data (Figure 4 (c), bottom). This porosity distribution might occur due to imperfect powder spreading on this particular layer and confirms the utility of the witness specimen for detecting layered flaws of this type.

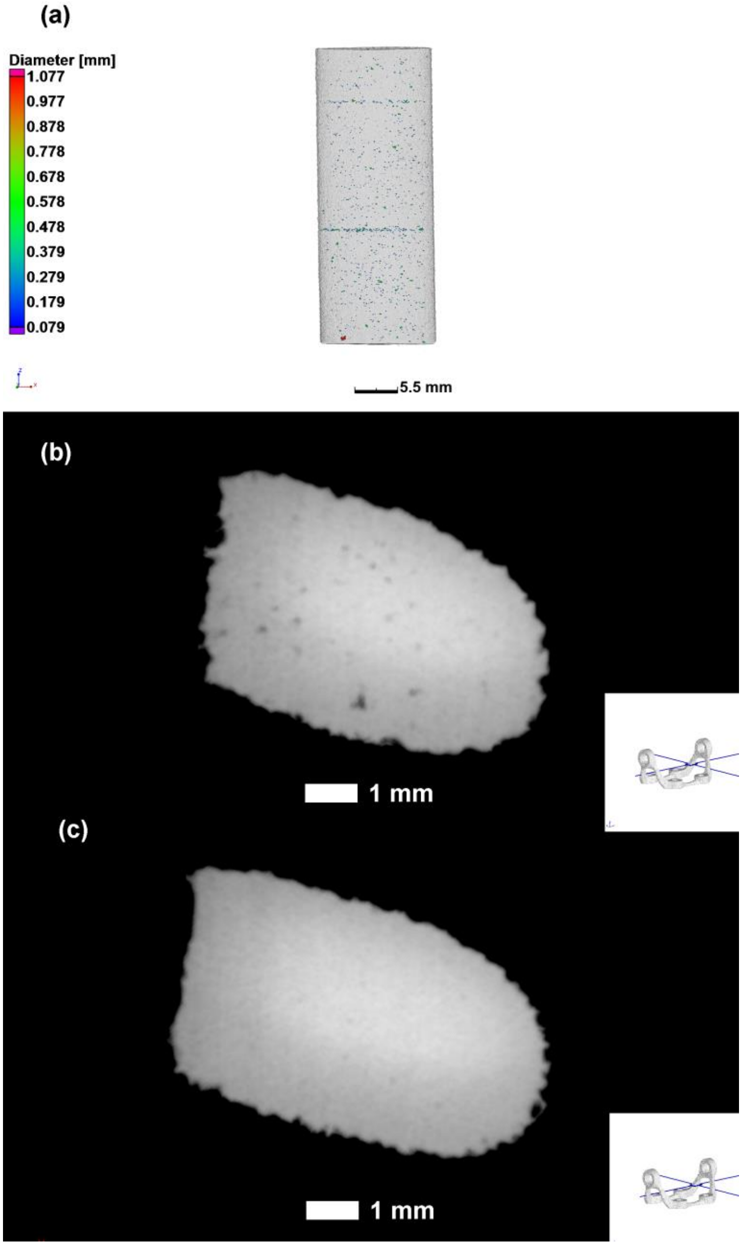

Figure 4: Layered lack of fusion porosity, presumably due to imperfect powder spreading – shown in (a) the witness specimen in 3D, and in the bracket by using carefully aligned slice images it is possible to image the pores (b)in the flaw plane and (c) out-of-plane in one arm of the bracket.

In addition to pores, contamination can occur in L-PBF systems such as from previous builds with different powder [33]. These inclusions can influence the melting process and act as stress concentrators in final parts under loading conditions. Such inclusions have different density, size and shape than the rest of the powder. Powder contamination also plays a potential role in the formation of porosity in L-PBF parts, since the inclusion particles have different melting temperature. It has been shown for example that during in-situ alloying with controlled amounts of different powders, the ideal process parameters change [34]. One set of parts in this series contained such inclusions as shown in Figure 5. This figure shows the detection of high density inclusions, which appear as white dots in both the witness specimen and bracket. Thus, the manufacturing of witness samples is useful for identifying negative features such as powder contamination, which is unacceptable in the manufacture of critical parts. In this case it was confirmed that contamination from a previous build was likely.

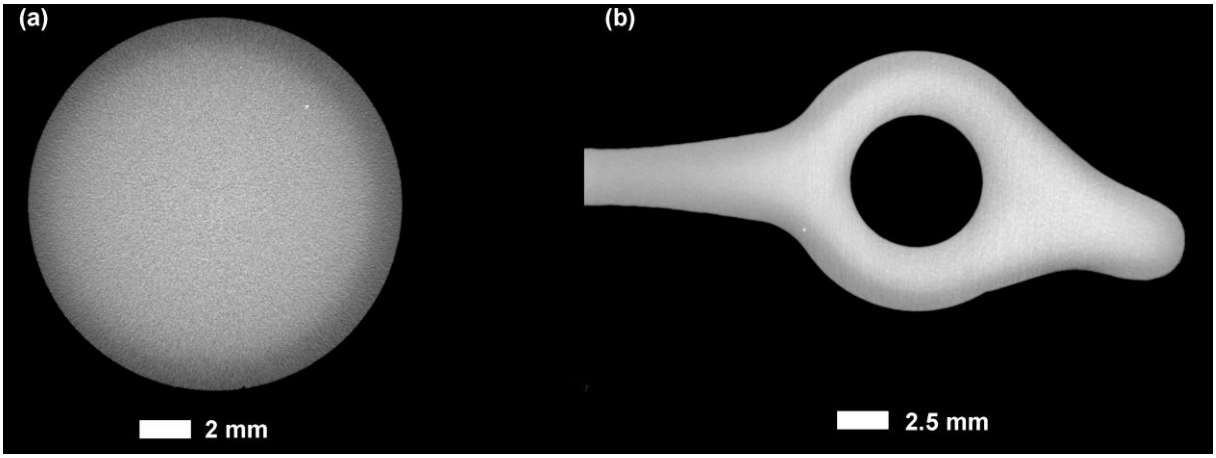

Figure 5: Inclusions (powder contamination) detected in (a) witness specimen and also in (b) the associated bracket – white dots seen in slice images are denser particles.

3.2 Stop-start flaw

Besides inherent process porosity, some errors can occur which create localized porosity or flaws, which can extend across the entire build plane or large parts of it. Of these, one of the most important is the stop-start flaw which occurs when there is a shutdown of the system and a restart later. This type of flaw is caused by shrinkage of the solidified part, which creates a larger layer height of powder in the next layer upon restart, which does not fully melt, thus leading to a specialized form of lack of fusion. A similar effect of imperfect melting on a single layer can occur when the laser power drops temporarily, or when powder spreading is uneven due to part warping or recoater damage, for example. Such effects may potentially be spread across the entire build, which means it may be detectable by using witness specimens. This is shown for an artificially induced stop-start flaw in a witness rod in Figure 6.

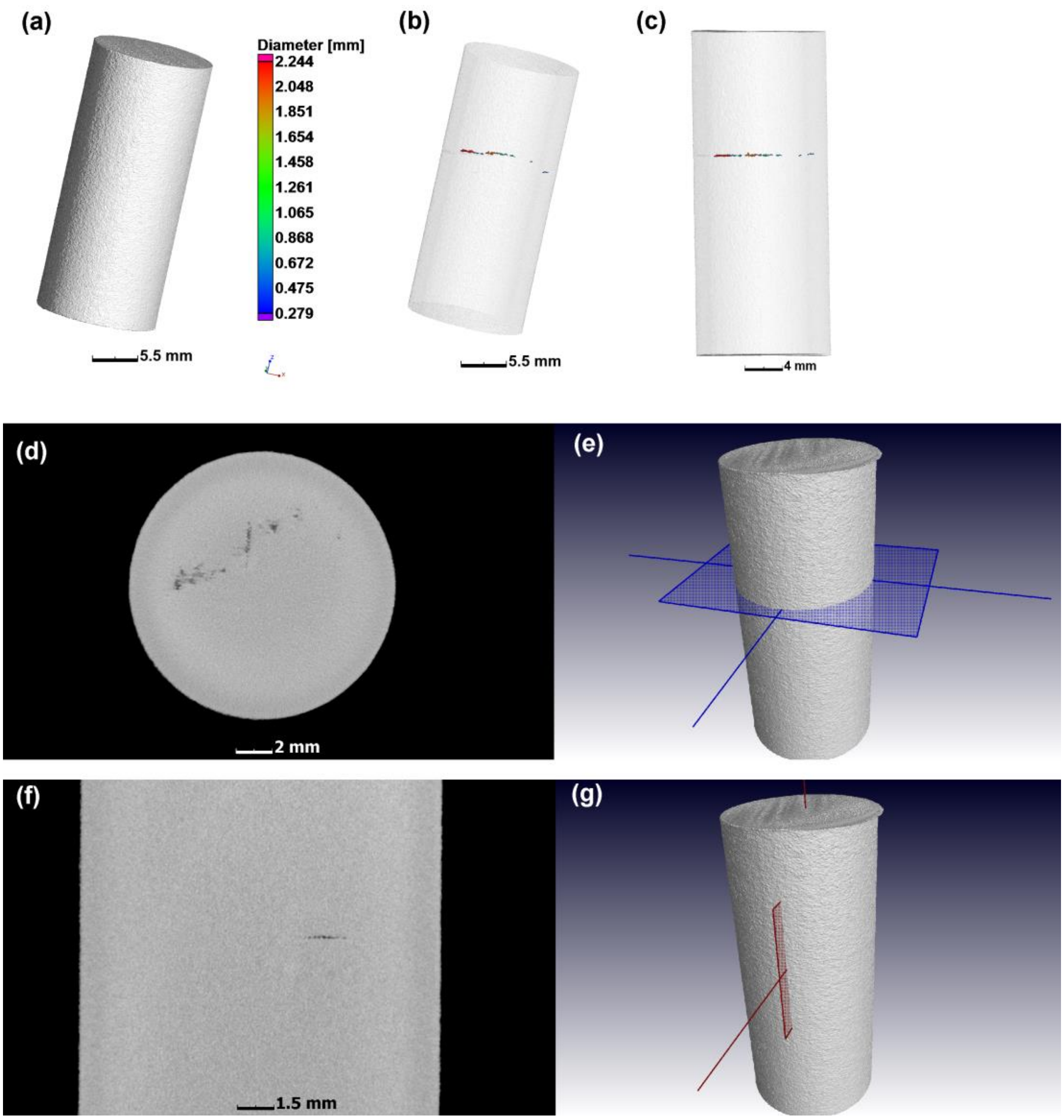

Figure 6: Stop-start flaw detected in witness specimen, different views of (a) 3D surface, (b) transparent angled view, (c) transparent side view, (d) slice top view in plane of flaw, (e) with the associated slice plane indicated, (f) slice side view and (g) associated slice plane indicated.

Detecting a start-stop flaw or other type of layer defect in a production part at the same height as the flaw which was observed in the corresponding witness specimen (Figure 6) can be problematic for X-ray tomography. In this case, despite a stop-start interval of 12 hrs (the machine was stopped during the build and restarted the next day), no layer defects were found inside the complex part (bracket) at the 46-µm resolution of the bracket scan. A higher resolution "zoom scan" of the bracket at 23-µm voxel size of the potentially problematic area corresponding to the known build height and build orientation where the build was stopped and restarted is shown in Figure 7.

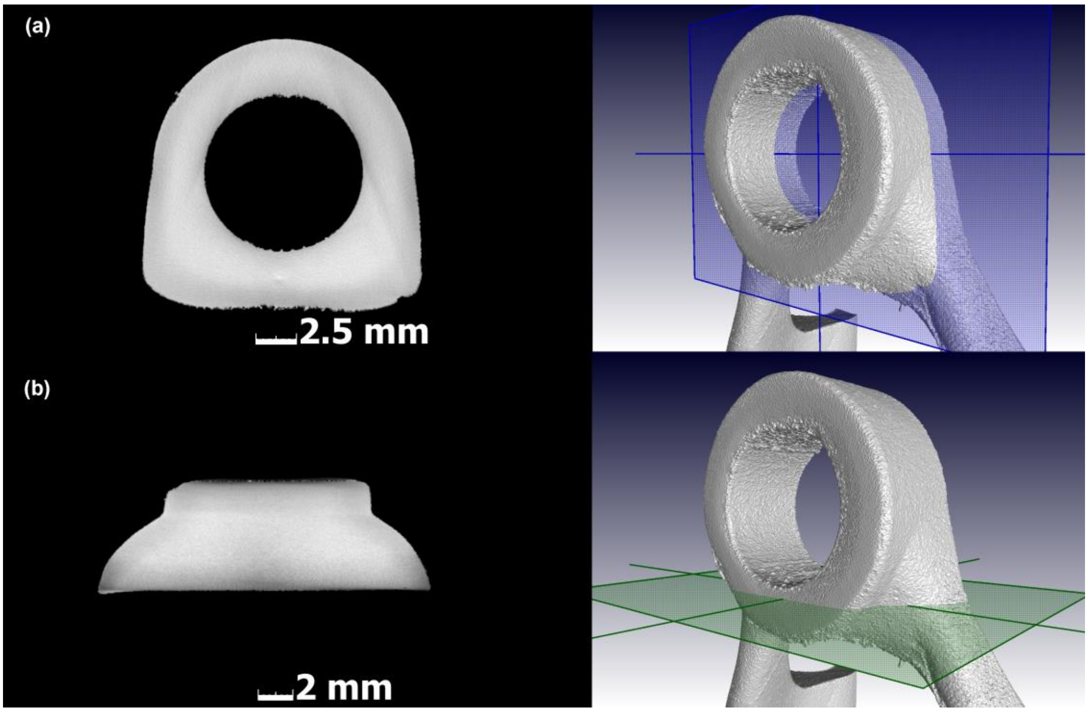

Figure 7: High resolution “zoom scan” of a potentially problematic area, corresponding to stop-start layer defect in a witness rod at a known z-height in the build. No layer defects were found in this case (23-µm resolution). Shown here are (a) the cross sectional (side) view and (b) top view in plane of expected location of layered defects (13 mm from top as measured from witness specimen).

However, no layer defects were found in this area or elsewhere in the build plane corresponding to the location of the stop-start flaw. The bracket was also sectioned and no flaws were found under nominal magnification with an optical microscope. Stop-start flaws may not be present in all locations in the build plane, as also seen in the witness specimen (the defect does not cover the entire area of the cylinder), and in this case they did not extend into the bracket.

The detection of planar 2D-flaws in AM parts perpendicular to the build (Z) direction is inherently challenging for any NDE technique, including microCT. As pointed out in [35], AM processes tend to prohibit volumetric defects with significant height in the Z direction. The major concern, therefore, is for planar defects, such as aligned or chained porosity or even laminar cracks, or the stop/start defects as examined in this paper, that form along the build plane. The implications of this are: 1) planar defects are well suited for growth, 2) planar defects generally have low contained volume, 3) the orientation of defects of concern must be known before inspection, especially when detection sensitivity depends on the defect orientation relative to the inspection direction, and 4) the Z-height of planar defects can be demanding on incremental step inspection methods such as CT. Therefore, it is important to manually assess slice images in microCT data from at least 2 orthogonal orientations and it is critical that the part is scanned at an angle relative to its original build direction. Regardless, when a larger production part cannot be inspected at sufficiently high resolution due to size limits, and layer or planar defects are positively identified in a smaller matching witness coupon, it would be safer to assume the presence of undetected layer defects in the production part and reject the part.

Microscopic analysis of physical cross-sections of the cylinder shows that the stop-start layered defect is comprised of a chain of pores with irregular shapes. Large irregular pores were found with vertical sizes ranging from 120 to 180 μm with narrow (up to 20 μm) shrinkage cavities. Usually, big irregular pores correlate with low energy input, when laser power density was not enough to fully melt the powder layer and previously melted material (also known as lack-of-fusion). Taking into account the 30-μm powder layer thickness used in this experiment, and the optimal process parameters needed to produce a fully dense part, the reason large stop-start defects occurred in the witness rod in this case can be attributed to shrinkage of the whole system during cooling, including the powder delivering system, baseplate and as-built part which had been previously melted in the first cycle prior to machine stoppage. The redistribution of residual stresses, detaching from the substrate or the warping of parts during cooling for several hours can lead to uneven layer thickness when the next powder layer is delivered. So, interaction of all these factors can lead to random porosity in L-PBF parts after a stop-start cycle, as was found in this experiment and as revealed by the presence of horizontally aligned pores in the witness rod (Figs. 6 and 8). The same defects were expected in the bracket but were absent (Fig. 7, 8(b) at the arrows). . In this stop-start L-PBF process, defects occurred along several layers taking into account their size (Fig. 8a) but despite this, the extent was not across the entire build plane and did not extend into the bracket.

As previously stated, the interaction of the microstructure and different types of porosity can be critical for the performance properties of the L-PBF part [36]. The interruption of the microstructural grain growth (in Ti6Al4V prior beta-gains grow typically vertical along the build direction) makes for possible new locations of crack initiation and growth along the inner (top and bottom) edges of the flaw along the vertical grain boundaries ending at the flaw.

Sharp edges of pores interrupted by prior-beta grains and notches coinciding with the direction of acicular martensitic α' phase (Fig. 8a) can influence not only the crack initiation under loading but can also deteriorate the fatigue performance of as-built and stress-relieved L-PBF components. Textured microstructure related to anisotropic structural properties usually remains even after heat treatment, for example, in Ti6Al4V [5,37].

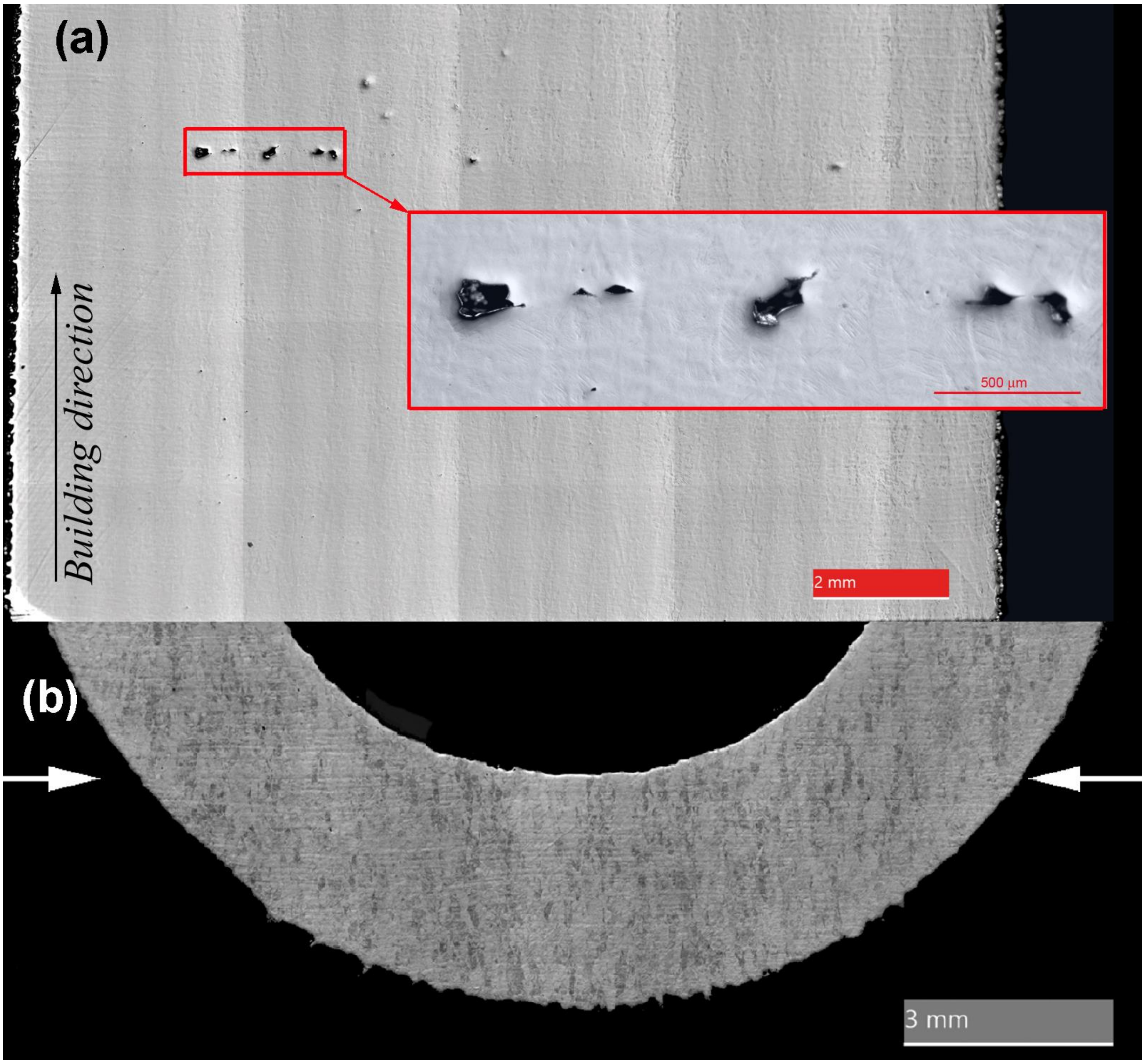

Figure 8: Cross section and microstructure of cylinder with layered defects (a) and part of the bracket where layered flaw was expected but was not found at location indicated by white arrows (b).

The advantages of the microCT inspection of witness specimens using standardized workflows has been clearly demonstrated in this work. The inherent disadvantage is that some layered flaws or irregular porosity distributions may occur in a complex part but not in the witness specimen. This means that the microCT inspection should be complimented by other inline process monitoring and post-process quality control tools. The shape and size of witness specimens, their position near the complex L-PBF component and the extent of layered flaws across the build plane justify a separate study in future.

For denser metals the method will need some modification compared to that presented here. The work in this paper was presented for Ti6Al4V and will be suitable for less radiodense materials (e.g., Al alloys, plastics, etc.). For denser materials, a narrower/finer witness specimen may be required to allow penetration of typical laboratory microCT X-ray beams. Also, it is imperative that the orientation of defects of concern is known before inspection to maximize CT detectability of known or suspected planar flaws. This means the build/print direction must be known and part angled relative to this, to ensure proper detection of the layered flaws in build plane. For larger L-PBF parts, the Z-height of planar defects such as the stop-start flaw examined here can be demanding on incremental step inspection methods such as CT. Nevertheless, this method should be useful for routine analysis with the only modification being the resolution of the scan of the complex part, which in turn depends on part size. The standardization of witness specimen geometry (e.g., uniform coupon diameter) allows a fixed methodology for all identically shaped additively manufactured witness specimens, regardless of the AM platform used, machine-to-machine variation, or variation within a single AM machine. The only limitation is that larger parts will require longer witness specimens, which will require longer scan times to identify flaws with the requisite resolution (≤ 20-µm voxel size in this paper). The advantage is that only one witness specimen may be adequate for an entire batch of parts to ensure the absence of unwanted layer, cross-layer, or other volumetric defect types (e.g., inclusions, trapped powder, cracks, etc.).

Conclusions

The advantages of using witness specimens and microCT scanning thereof according to fixed workflows was investigated. It was shown how this approach can accurately identify process porosity signatures, which can act as “witness” to in-process changes in the parameters over a single layer or multiple layers. The presence of contamination of metal powders was demonstrated in one case and this was accurately detected in both a witness specimen and its corresponding complex part. Lack of fusion porosity detected in a witness specimen was found to occur across multiple build layers in one case, and analogous lack of fusion porosity was confirmed in the complex bracket associated with this witness specimen. Finally, an artificially induced stop-start flaw was investigated and its detection in witness specimen confirmed and analysed in detail using microCT and optical microscopy of cross-sections. This stop-start flaw was found to extend widely but not completely over the entire part, and in this case, did not extend to the complex part built alongside it (also investigated by microCT and optical microscopy). This points to the possibility that unexpected flaws including layered flaws may occur in complex parts despite passing a witness specimen microCT test. Similarly, there may be situations where localized power fluctuations occur or where build quality varies with location in the powder bed. This means that additional complementary tools are needed for 100% quality control and understanding the limits of the microCT technique to detect planar defects is therefore important. This work is expected to contribute to the wider understanding and better utility of microCT as inspection tool, especially with standardized workflows using witness specimens.

Acknowledgements

The Collaborative Program for Additive Manufacturing (CPAM), funded by the South African Department of Science and technology, is acknowledged for financial support. This work is also based on the research supported by the South African Research Chairs Initiative of the Department of Science and Technology and National Research Foundation of South Africa (Grant № 97994). Samples were built in CRPM at Central University of Technology, Free State.

References

[1] M. Schmidt, M. Merklein, D. Bourell, D. Dimitrov, T. Hausotte, K. Wegener, L. Overmeyer, F. Vollertsen, G.N. Levy, Laser based additive manufacturing in industry and academia, CIRP Ann. 66 (2017) 561–583. doi:10.1016/J.CIRP.2017.05.011.

[2] T. DebRoy, T. Mukherjee, J.O. Milewski, J.W. Elmer, B. Ribic, J.J. Blecher, W. Zhang, Scientific, technological and economic issues in metal printing and their solutions, Nat. Mater. (2019) 1. doi:10.1038/s41563-019-0408-2.

[3] T. Wohlers, T. Caffrey, R.I. Campbell, O. Diegel, J. Kowen, Wohlers Report 2018: 3D Printing and Additive Manufacturing State of the Industry, 2018.

[4] T. Debroy, H.L. Wei, J.S. Zuback, T. Mukherjee, J.W. Elmer, J.O. Milewski, A.M. Beese, A. Wilson-Heid, A. De, W. Zhang, Additive manufacturing of metallic components – Process, structure and properties, Prog. Mater. Sci. 92 (2018) 112–224. doi:10.1016/j.pmatsci.2017.10.001.

[5] I. Yadroitsev, P. Krakhmalev, I. Yadroitsava, A. Du Plessis, Qualification of Ti6Al4V ELI Alloy Produced by Laser Powder Bed Fusion for Biomedical Applications, JOM. 70 (2018) 372–377. doi:10.1007/s11837-017-2655-5.

[6] M. Qian, W. Xu, M. Brandt, H.P. Tang, Additive manufacturing and postprocessing of Ti-6Al-4V for superior mechanical properties, MRS Bull. 41 (2016) 775–784. doi:10.1557/mrs.2016.215.

[7] H. Gong, K. Rafi, H. Gu, T. Starr, B. Stucker, Analysis of defect generation in Ti-6Al-4V parts made using powder bed fusion additive manufacturing processes, Addit. Manuf. 1 (2014) 87–98. doi:10.1016/j.addma.2014.08.002.

[8] A. du Plessis, Effects of process parameters on porosity in laser powder bed fusion revealed by X-ray tomography, Addit. Manuf. 30 (2019) 100871. doi:10.1016/j.addma.2019.100871.

[9] L. Cordova, M. Campos, T. Tinga, Revealing the Effects of Powder Reuse for Selective Laser Melting by Powder Characterization, JOM. 71 (2019) 1062–1072. doi:10.1007/s11837-018-3305-2.

[10] I. Yadroitsava, I. Yadroitsev, Residual stress in metal specimens produced by direct metal laser sintering, in: Solid Free. Fabr. Symp., 2015: pp. 10–12. http://sffsymposium.engr.utexas.edu/sites/default/files/2015/2015-49-Yadroitsev.pdf.

[11] M. Kabir, H. Richter, Modeling of Processing-Induced Pore Morphology in an Additively-Manufactured Ti-6Al-4V Alloy, Materials (Basel). 10 (2017) 145. doi:10.3390/ma10020145.

[12] A. du Plessis, I. Yadroitsev, I. Yadroitsava, S.G. Le Roux, X-Ray Microcomputed Tomography in Additive Manufacturing: A Review of the Current Technology and Applications, 3D Print. Addit. Manuf. 5 (2018) 3dp.2018.0060. doi:10.1089/3dp.2018.0060.

[13] E. Maire, P.J. Withers, Quantitative X-ray tomography, Int. Mater. Rev. 59 (2014) 1–43. doi:10.1179/1743280413Y.0000000023.

[14] A. Thompson, I. Maskery, R.K. Leach, X-ray computed tomography for additive manufacturing: a review, Meas. Sci. Technol. 27 (2016) 072001. doi:10.1088/0957-0233/27/7/072001.

[15] F.H. Kim, S.P. Moylan, E.J. Garboczi, J.A. Slotwinski, Investigation of pore structure in cobalt chrome additively manufactured parts using X-ray computed tomography and three-dimensional image analysis, Addit. Manuf. 17 (2017) 23–38. doi:10.1016/J.ADDMA.2017.06.011.

[16] A. du Plessis, S.G. le Roux, G. Booysen, J. Els, Directionality of Cavities and Porosity Formation in Powder-Bed Laser Additive Manufacturing of Metal Components Investigated Using X-Ray

Tomography, 3D Print. Addit. Manuf. (2016). doi:10.1089/3dp.2015.0034.

[17] H. Villarraga-Gómez, C. Lee, S.T. Smith, Dimensional metrology with X-ray CT: A comparison with CMM measurements on internal features and compliant structures, Precis. Eng. 51 (2018) 291–307. doi:10.1016/J.PRECISIONENG.2017.08.021.

[18] H. Villarraga-Gómez, E.L. Herazo, S.T. Smith, Progression of X-ray computed tomography from medical imaging to current status in dimensional metrology, Precis. Eng. (2019). doi:10.1016/J.PRECISIONENG.2019.06.007.

[19] M. Seifi, A. Salem, J. Beuth, O. Harrysson, J.J. Lewandowski, Overview of Materials Qualification Needs for Metal Additive Manufacturing, JOM. 68 (2016) 747–764. doi:10.1007/s11837-015-1810-0.

[20] A. du Plessis, P. Sperling, A. Beerlink, L. Tshabalala, S. Hoosain, N. Mathe, G. Stephan, MethodsX Standard method for microCT-based additive manufacturing quality control 1 : Porosity analysis, MethodsX. 5 (2018) 1102–1110. doi:10.1016/j.mex.2018.09.005.

[21] A. du Plessis, P. Sperling, A. Beerlink, L. Tshabalala, S. Hoosain, N. Mathe, G. Stephan, MethodsX Standard method for microCT-based additive manufacturing quality control 2 : Density measurement, MethodsX. 5 (2018) 1117–1123. doi:10.1016/j.mex.2018.09.006.

[22] A. du Plessis, P. Sperling, A. Beerlink, O. Kruger, L. Tshabalala, S. Hoosain, S.G. le Roux, Standard method for microCT-based additive manufacturing quality control 3: Surface roughness, MethodsX. 5 (2018) 1111–1116. doi:10.1016/j.mex.2018.09.006.

[23] A. du Plessis, P. Sperling, A. Beerlink, W. du Preez, S.G. le Roux, Standard method for microCT-based additive manufacturing quality control 4: Metal powder analysis, MethodsX. 5 (2018) 1336–1345. doi:10.1016/j.mex.2018.09.006.

[24] ASTM WK47031, “Standard Guide for Nondestructive Testing of Metal Aerospace Additive Manufactured Parts After Build", (2019). https://www.astm.org/WorkItems/WK47031.htm, last accessed May 23, 2019.

[25] ISO/ASTM DTR 52905 (ASTM F42) Additive manufacturing -- General principles -- Non-destructive testing of additive manufactured products, under development, ISO Technical Committee 261 (2019)., 2019. https://www.iso.org/standard/71988.html, last accessed May 23, 2019.

[26] A. Du Plessis, S.G. Le Roux, J. Els, G. Booysen, D.C. Blaine, Application of microCT to the non-destructive testing of an additive manufactured titanium component, Case Stud. Nondestruct. Test. Eval. 4 (2015) 1–7. doi:10.1016/j.csndt.2015.09.001.

[27] M. Seifi, M. Gorelik, J. Waller, N. Hrabe, N. Shamsaei, S. Daniewicz, J.J. Lewandowski, Progress Towards Metal Additive Manufacturing Standardization to Support Qualification and Certification, JOM. 69 (2017) 439–455. doi:10.1007/s11837-017-2265-2.

[28] AWS Bookstore. D20.1/D20.1M:2019 SPECIFICATION FOR FABRICATION OF METAL COMPONENTS USING ADDITIVE MANUFACTURING, (n.d.). https://pubs.aws.org/p/1915/d201d201m2019-specification-for-fabrication-of-metal-components-using-additive-manufacturing (accessed September 17, 2019).

[29] A. du Plessis, S.G. le Roux, Standardized X-ray tomography testing of additively manufactured parts: A round robin test, Addit. Manuf. 24 (2018) 125–136. doi:10.1016/j.addma.2018.09.014.

[30] A. du Plessis, S.G. le Roux, A. Guelpa, The CT Scanner Facility at Stellenbosch University: An

open access X-ray computed tomography laboratory, Nucl. Instruments Methods Phys. Res. Sect. B Beam Interact. with Mater. Atoms. 384 (2016) 42–49. doi:10.1016/J.NIMB.2016.08.005.

[31] A. Du Plessis, S.G. Le Roux, G. Booysen, J. Els, Quality Control of a Laser Additive Manufactured Medical Implant by X-Ray Tomography, 3D Print. Addit. Manuf. 3 (2016) 175–182. doi:10.1089/3dp.2016.0012.

[32] C.H. Hands, A. du Plessis, N. Minnaar, B.A. Blakey-Milner, E. Burger, Can Additive Manufacturing Help Win the Race?, (2018). doi:10.20944/PREPRINTS201811.0040.V1.

[33] A.D. Brandão, R. Gerard, J. Gumpinger, S. Beretta, A. Makaya, L. Pambaguian, T. Ghidini, Challenges in Additive Manufacturing of space parts: Powder feedstock cross-contamination and its impact on end products, Materials (Basel). 10 (2017). doi:10.3390/ma10050522.

[34] P. Krakhmalev, I. Yadroitsev, Microstructure and properties of intermetallic composite coatings fabricated by selective laser melting of Ti–SiC powder mixtures, Intermetallics. 46 (2014) 147–155. doi:10.1016/J.INTERMET.2013.11.012.

[35] Standard for Additively Manufactured Spaceflight Hardware by Laser Powder Bed Fusion in Metals, MSFC-STD-3716, NASA Marshall Spaceflight Center, Huntsville, AL, October 18, 2017, (n.d.).

[36] S. Liu, Y.C. Shin, Additive manufacturing of Ti6Al4V alloy: A review, Mater. Des. 164 (2019) 107552. doi:10.1016/J.MATDES.2018.107552.

[37] P. Barriobero-Vila, J. Gussone, A. Stark, N. Schell, J. Haubrich, G. Requena, Peritectic titanium alloys for 3D printing, Nat. Commun. 9 (2018) 3426. doi:10.1038/s41467-018-05819-9.